Journal of Materials Chemistry

Cite this: J. Mater. Chem., 2012, 22, 14633

www.rsc.org/materials

PAPER

High-temperature charge transport and thermoelectric properties of a degenerately Al-doped ZnO nanocomposite

Woo Hyun Nam,[ab] Young Soo Lim,*[a] Soon-Mok Choi,[a] Won-Seon Seo[a] and Jeong Yong Lee*[b]

Received 21st March 2012, Accepted 16th May 2012
DOI: 10.1039/c2jm31763j

2 mol% Al-doped ZnO nanoparticles were consolidated into a ZnO nanocomposite with $ZnAl_2O_4$ nanoprecipitates by spark plasma sintering and its high-temperature charge transport and thermoelectric properties were investigated up to 1073 K. The carrier concentration in the nanocomposite was not dependent on the temperature, while the Hall mobility showed positive temperature-dependence due to grain boundary scattering. The negative Seebeck coefficient of the nanocomposite was linearly proportional to the temperature, and the density of the state effective mass (m_d*) was evaluated to be $0.33m_e$ by using the Pisarenko relation. Drastic reduction of thermal conductivity ($k < 2$ W m^{-1} K^{-1}) was achieved in the nanocomposite, and the maximum ZT of 0.34 was obtained at 1073 K.

Introduction

Recently, thermoelectric research for power generation from waste heat has been explosively renewed due to increasing global concern for energy and environmental issues.[1–3] The waste heat can be directly converted into electric power by the thermoelectric generation and its efficiency is mainly governed by the properties of thermoelectric materials. Since the first report on its thermoelectric properties by Ohtaki's group,[4] ZnO has attracted considerable attention as a n-type oxide thermoelectric material due to its abundance, non-toxicity, and low cost. The performance of a thermoelectric material is determined by the dimensionless figure of merit, $ZT = S^2\sigma T/\kappa$, where S, σ, T and κ are Seebeck coefficient, electrical conductivity, absolute temperature and thermal conductivity, respectively. Therefore, the reduction of the thermal conductivity without significant loss of power factor ($S^2\sigma$) is strongly demanded for the enhancement of the thermoelectric performance.

In a ZnO thermoelectric materials system, phonon scattering mechanisms, such as impurity scattering by dual doping and grain boundary scattering by nanostructuring, have been successfully applied to the thermal conductivity reduction.[5–7] Ohtaki *et al.* reported the highest ZT of 0.65 at 1247 K in $Zn_{0.96}Al_{0.02}Ga_{0.02}O$ and it is the best ZT value in n-type bulk oxide thermoelectric materials to date.[5] Kinemuchi *et al.* observed drastic reduction of thermal conductivity ($k < 5$ W m^{-1} K^{-1}) in undoped ZnO nanocomposites by the grain boundary scattering,[6] and Jood *et al.* could reduce the thermal conductivity even further ($k < 2$ W m^{-1} K^{-1}) in an Al-doped ZnO nanocomposite containing uniformly distributed $ZnAl_2O_4$ nanoprecipitates.[7]

Despite the significant achievements in the thermal conductivity reduction, the high-temperature charge transport mechanism in a ZnO nanocomposite has not yet been fully understood. At room-temperature and below, the charge transport mechanism in ZnO has been extensively investigated for the transparent conducting oxide applications.[8–10] Electrons can be scattered by grain boundary, lattice vibration and ionized impurity, and the main scattering mechanism is determined by the temperature and the carrier concentration in ZnO.[11,12] Because the thermoelectric phenomenon is governed by the transport mechanisms of both electrons and phonons, understanding the high-temperature charge transport mechanism is of great importance for further improvement of ZnO thermoelectric materials.

In this work, we report the high-temperature charge transport and thermoelectric properties of a degenerately Al-doped ZnO nanocomposite. The ZnO nanocomposite was prepared by the spark plasma sintering of Al-doped ZnO nanoparticles. Charge transport properties in the nanocomposite were characterized up to 1073 K by using a Hall measurement system, and grain boundary scattering was found to be the main electron scattering mechanism. The relation between the charge transport and thermoelectric properties in the nanocomposite was discussed and it could be interpreted by using the classical Pisarenko relation. Besides, the impacts of the nanostructuring on the thermal conductivity in thermoelectric ZnO were also discussed.

[a]*Green Ceramics Division, Korea Institute of Ceramic Engineering and Technology, 233-5 Gasan-dong, Geumcheon-gu, Seoul 153-801, Republic of Korea. E-mail: yslim@kicet.re.kr*
[b]*Department of Materials Science and Engineering, Korea Advanced Institute of Science and Technology, 373-1 Guseong-dong, Yuseong-gu, Daejeon 305-701, Republic of Korea. E-mail: j.y.lee@kaist.ac.kr*

Experimental

Synthesis

2 mol% Al-doped ZnO nanoparticles were synthesized *via* a solution method using zinc nitrate hexahydrate ($Zn(NO_3)_2 \cdot 6H_2O$), hexamethylenetetramine ($(CH_2)_6N_4$), and aluminum nitrate nonahydrate ($Al(NO_3)_3 \cdot 9H_2O$) as dopant materials. The zinc nitrate hexahydrate and the hexamethylenetetramine have been extensively used as agents for the formation of ZnO nanoparticles.[13,14] 7.288 g (0.049 M) of zinc nitrate hexahydrate, 35.048 g (0.5 M) of hexamethylenetetramine, 0.188 g (0.001 M) of aluminum nitrate nonahydrate were dissolved in 500 ml of deionized water in a beaker, and then the above solution was heated to 80 °C for 1 h on a hot plate. When the reaction was completed, the solution was cooled naturally to room temperature. The white precipitate was separated by centrifuging, washed with ethanol and deionized water, and finally dried in an oven at 100 °C for 6 h. The Al-doped ZnO nanoparticles were consolidated into the nanocomposite by spark plasma sintering. The nanoparticles (3.5 g) were loaded into a graphite mold and placed into the sintering chamber. The mold was heated up to 900 °C at the heating rate of 100 °C min^{-1} and held for 5 min in a vacuum. During the heating and sintering process, a uniaxial constant pressure of 50 MPa was applied. Then, the pressure was released, and the sample was furnace quenched to room temperature. Graphite foils were used to transmit electric current effectively to the sample during the spark plasma sintering. After the sintering process, the graphite foils were completely removed by using a diamond cutter. The diameter and the height of the sintered body were 12.5 mm and 6 mm, respectively.

Characterization

The crystal structure of the Al-doped ZnO nanoparticle was characterized by using an X-ray diffractometer (XRD, Rigaku, D/MAX-3C) with Ni filtered Cu Kα radiation. The operation voltage and current were kept at 40 kV and 45 mA, respectively. Microstructural properties of the nanoparticle and the nanocomposite were characterized by using a scanning transmission electron microscope (STEM, Hitachi, HD-2300A) operating at an acceleration voltage of 200 kV. To analyze the elemental distribution in the nanoparticle and the nanocomposite, energy dispersive X-ray spectroscopy (EDS) line scan and elemental mapping were performed during the STEM measurement. Furthermore, a high-resolution transmission electron microscopy (HRTEM) study was performed in a JEOL JEM-4010 to investigate the second phase in the nanocomposite. Electrical conductivity and Seebeck coefficient were measured by using a thermoelectric property measurement system (TPMS, Ozawa Science, RZ-2001i) with a four-probe method. High-temperature charge transport properties were characterized up to 1073 K by using a high-temperature Hall measurement system (HT-Hall, Toyo Corporation, ResiTest 8400) under a magnetic field of 0.57 T. Thermal conductivity was measured by using a laser flash method (NETZSCH, LFA-457).

Results and discussion

Microstructural properties of the degenerately Al-doped ZnO nanocomposite

Fig. 1(a) shows the XRD pattern of the 2 mol% Al-doped ZnO nanoparticles. The XRD pattern reveals that all peaks correspond to a hexagonal wurtzite structure (JCPDS card no. 36-1451). The lattice parameters calculated from the XRD pattern are $a = 3.265$ Å and $c = 5.229$ Å. These values are slightly greater than the JCPDS values for undoped ZnO powder ($a = 3.250$ Å and $c = 5.207$ Å). The increase in the lattice parameters of the Al-doped nanoparticles is related to the incorporation of Al^{3+} ions into Zn^{2+} sites and interstitial positions.[15,16] No traces of any secondary phases or other impurities were detected, indicating that the nanoparticles consist of a single wurtzite phase. Fig. 1(b) represents a STEM micrograph of the nanoparticles. This figure clearly shows that nano-sized ZnO particles (average size: ~90 nm) were synthesized by the solution method. The corresponding EDS elemental mapping images of Zn, O, and Al are represented in Fig. 1(c)–(e), respectively. These figures illustrate the distribution of the individual elements of Zn, Al, and O in the nanoparticles, showing that the Al dopant is uniformly distributed in the nanoparticles.

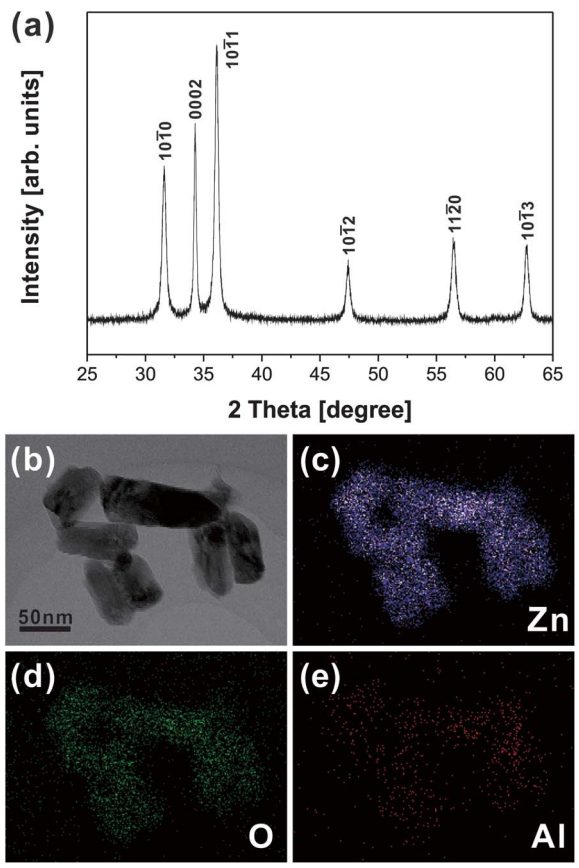

Fig. 1 (a) An XRD pattern of the 2 mol% Al-doped ZnO nanoparticle. (b) A STEM micrograph of the nanoparticles. (c), (d), and (e) are the corresponding EDS elemental mapping results of Zn, O, and Al, respectively.

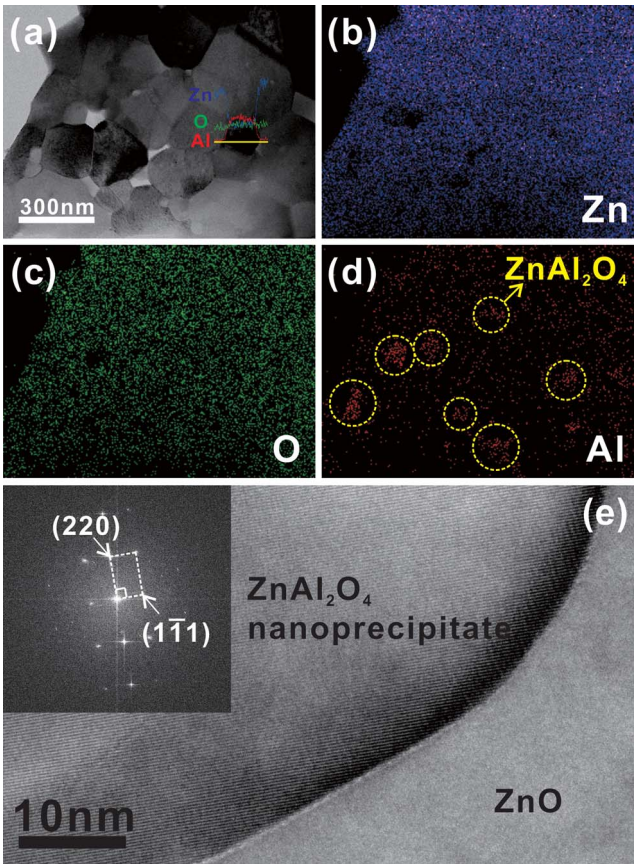

Fig. 2 (a) A STEM micrograph of the Al-doped ZnO nanocomposites and EDS line profile of Zn, O, and Al. (b), (c), and (d) are the corresponding EDS elemental mapping results of Zn, O, and Al, respectively. $ZnAl_2O_4$ nanoprecipitates are marked by yellow circles in (d). (e) A HRTEM micrograph of a $ZnAl_2O_4$ nanoprecipitate and the corresponding FFT image (inset).

A STEM micrograph of the nanocomposite is shown in Fig. 2(a). In comparison with other sintering methods, the spark plasma sintering enables ZnO nanoparticles to be densely consolidated into the nanocomposite with suppressed grain growth due to the simultaneous application of pressure and electric current on the nanoparticles in a short process time.[7,17–19] The average grain size in the nanocomposite was ~200 nm and the relative density was 94%. An EDS line scan was performed along the yellow line in Fig. 2(a), and the resulting profile of Zn, O, and Al indicates formation of an Al-rich phase. This result indicates that $ZnAl_2O_4$ nanoprecipitates were formed during the spark plasma sintering process. Fig. 2(b)–(d) show corresponding EDS elemental mapping images of Zn, O, and Al, respectively. In agreement with the EDS line scan result, the EDS elemental mapping images in Fig. 2(b)–(d) also revealed that the $ZnAl_2O_4$ nanoprecipitates (average size: ~100 nm, marked by yellow circles in Fig. 2(d)) were produced in the nanocomposite.[4,7] The crystal structure of the nanoprecipitate was also proven to be $ZnAl_2O_4$ by using the HRTEM micrograph in Fig. 2(e) and its Fast Fourier Transformation (FFT) image in the inset. The nanoprecipitates were distributed over the whole area of the nanocomposite. The effect of the nanoprecipitates on the charge and thermal transport in the ZnO nanocomposite will be discussed below.

Charge transport properties of the degenerately Al-doped ZnO nanocomposite

Electrical conductivities of the ZnO nanocomposite were independently characterized by using TPMS and HT-Hall measurements as shown in Fig. 3(a). They showed almost the same tendency and quite similar values ($\Delta\sigma < 6\%$). Rapid increase of the electrical conductivity was obviously observed above ~723 K, while the increase of the electrical conductivity was not significant below that temperature. The transition of the electrical conductivity at around 723 K was also observed in a recent article, but the authors regarded the increase of carrier concentration as the origin of the semiconducting behavior at the relatively high temperature.[4] However, the HT-Hall measurement revealed that the carrier concentration in the nanocomposite was not strongly dependent on the temperature (Fig. 3(b)). Regardless of the temperature, the carrier concentration was almost constant. Its average value was 6.8×10^{19} cm^{-3} and it satisfied the criteria of the degenerate ZnO semiconductor ($n > 3.7 \times 10^{18}$ cm^{-3}).[11] Considering the amount of Al dopants (2 mol%), the carrier concentration in the nanocomposite was one order lower than the theoretical carrier concentration ($n = 7.4 \times 10^{20}$ cm^{-3}). Firstly, the formation of the $ZnAl_2O_4$ spinel phase observed in Fig. 2 can be one reason as reported by Tsubota *et al.* ($n = 7.2 \times 10^{19}$ cm^{-3} in 2 mol% Al-doped ZnO).[20] Secondly, because the Hall measurement can detect only in-grain carrier concentration, trapped electrons at grain boundary interfaces can be the other reason for the observed carrier concentration.[21]

Fig. 3(c) shows temperature-dependent Hall mobility of the nanocomposite. The mobility showed weak temperature dependence at relatively low temperature, but it rapidly increased above 723 K. As expected from the carrier concentration in Fig. 3(b), the temperature-dependent electrical conductivity was mainly governed by the mobility. Because the electrical conductivity in the nanocomposite was quite less than that reported by Ohtaki *et al.* in conventionally prepared 2 mol% Al-doped ZnO by solid state reaction between ZnO and Al_2O_3 powders,[4] grain boundary scattering can be regarded as the main scattering mechanism in the electron transport. In a polycrystalline semiconductor, Seto established a thermionic emission model for the scattering by the grain boundary barrier,[22] where the barrier height (Φ_B) can be obtained from the slope of $\ln(\mu T^{1/2})$ *vs.* $1/T$. Although it is invalid only for the non-degenerate case, this model has been widely applied to explain the transport mechanism in degenerately doped oxide semiconductors.[23,24] However, as clarified by Bruneaux *et al.*,[25] Fermi–Dirac statistics should be considered for degenerately doped semiconductors, and the temperature dependence of the mobility can be expressed as shown in eqn (1):

$$\mu = AT\exp\left(-\frac{\Phi_A}{kT}\right), \quad (1)$$

where A is a pre-exponent factor, which is dependent on the carrier concentration, effective mass and grain size, k is the Boltzmann constant, T is the absolute temperature, and

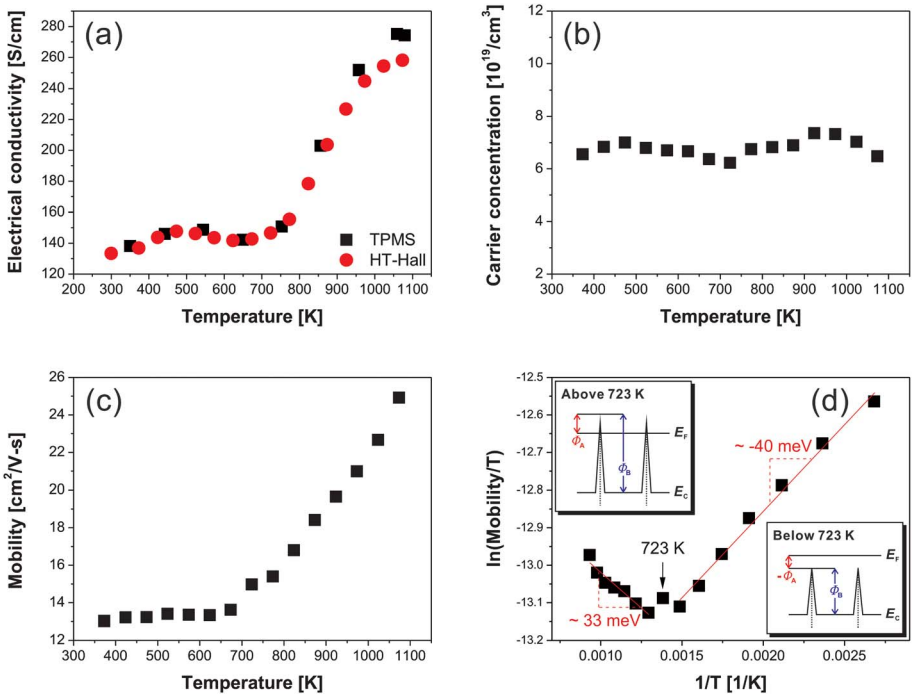

Fig. 3 Temperature-dependent (a) electrical conductivity, (b) carrier concentration, and (c) mobility of the Al-doped ZnO nanocomposite. (b) A plot of $\ln(\mu/T)$ *vs.* $1/T$ from the grain boundary scattering model by Bruneaux *et al.* This plot indicates temperature-dependence of the grain boundary barrier in the nanocomposite. The corresponding band structures of the nanocomposite are schematically represented in insets of (d). Dotted lines in the insets indicate the grain boundaries.

$\Phi_A = \Phi_B - (E_F - E_C)$ is an activation energy related to the grain boundary barrier height (Φ_B) and the energy difference between the Fermi level and the bottom of the conduction band in the neutral region ($E_F - E_C$). The activation energy, Φ_A, can be achieved from the slope of $\ln(\mu/T)$ *vs.* $1/T$ in Fig. 3(d). Below 723 K, it showed a negative slope of −40 meV. This result revealed that the Fermi level is higher than the barrier height, Φ_B. The difference between E_F and E_C was estimated by using a free electron model,[22] $\varepsilon_F = (3\pi^2 n)^{2/3}\hbar^2/2m_e = 183$ meV for $n = 6.8 \times 10^{19}$ cm^{-3} and $m_e = 0.33m_o$. Consequently, the grain boundary barrier height was found to be 143 meV. Despite its negative activation energy, very weak positive temperature dependence of the mobility was observed in this temperature range as shown in Fig. 3(c), and it can be attributed to the non-negligible grain boundary scattering as proposed by Prins *et al.*[26]

As temperature increased, the activation energy gradually increased and eventually became a positive value (~33 meV). It indicated that the degenerate Fermi level located between the conduction band maximum of the ingrain neutral region and the top of the grain boundary barrier. In this case, the grain boundary barrier height was 216 meV. A possible explanation for the temperature dependence of the grain boundary barrier height could be made by considering a grain boundary model in ZnO proposed by Gupta and Carlson. According to the model, the formation of negatively charged zinc vacancies at the grain boundary interface increases the barrier height.[27] Therefore, the evolution of the positive activation energy (Φ_A) above 723 K can be attributed to the changes in the space charge distribution around the grain boundary interface and it can be regarded as the reason for the transition in the electrical conductivity observed in Fig. 3(a). The temperature-dependent activation energy for the nanocomposite is schematically shown as band structures in insets of Fig. 3(d).

Thermoelectric properties of the degenerately Al-doped ZnO nanocomposite

The Seebeck coefficient of the degenerately Al-doped ZnO nanocomposite was characterized by using TPMS and the result is shown in Fig. 4(a). Negative Seebeck coefficients (−50 to −140 μV K^{-1}) were observed in the nanocomposite over the whole temperature range, and are in good agreement not only with the experimental results reported in a bulk ZnO,[20] but also with recent calculation based on Boltzmann transport theory.[28] Unlike the case of the electrical conductivity, the effect of grain boundaries in the nanocomposite on the Seebeck coefficient was not significant. Interestingly, the negative Seebeck coefficient was monotonously increasing with temperature. The linear relationship between S and T has also been observed in the literature, but the origin has not yet been reported.[4,7] The Seebeck coefficient can be expressed by using the Pisarenko relation in eqn (2):

$$S = \frac{8\pi^2 k^2 T}{3qh^2} m_d^* \left(\frac{\pi}{3n}\right)^{2/3}, \quad (2)$$

where h is Planck's constant, q is an electron charge and m_d* is a density of the state (DOS) effective mass at the Fermi level. Because the carrier concentration in the degenerately doped nanocomposite was not strongly affected by temperature as shown in Fig. 4(b), the Seebeck coefficient should be linearly proportional to the temperature when the DOS effective mass,

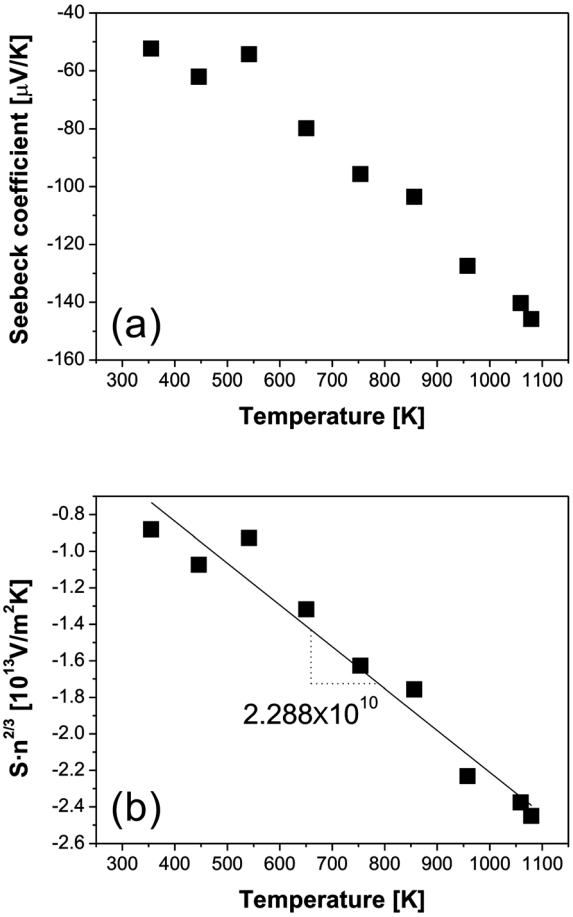

Fig. 4 (a) Temperature-dependence of the Seebeck coefficient for the Al-doped ZnO nanocomposite. The linear relationship between Seebeck coefficient and temperature is observed. (b) A plot of $Sn^{2/3}$ *vs.* T from the Pisarenko relation. The DOS effective mass can be calculated by using the slope of this plot.

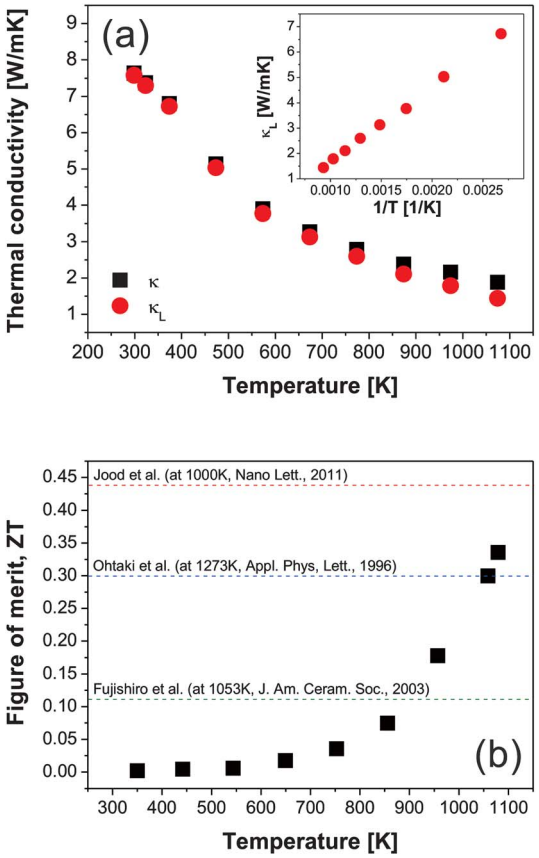

Fig. 5 (a) Temperature-dependent thermal conductivity and (b) dimensionless figure of merit of the Al-doped ZnO nanocomposite. The inset in (a) shows a plot of the lattice thermal conductivity *vs.* $1/T$. The highest ZT of 0.34 at 1073 K was achieved in the nanocomposite.

m_d*, is constant. Furthermore, the DOS effective mass can be measured by the slope of $Sn^{2/3}$ *vs.* T. The straight slope in Fig. 4(b) indicates that the effective mass in the nanocomposite is $0.332m_o$, and it is strikingly consistent with the result reported by Kim *et al.*[29] They measured the DOS effective masses in highly doped ZnO thin films by using the method of four coefficients (MFC), where Hall coefficient, Nernst coefficient, Seebeck coefficient and electrical conductivity are used for the measurement. The effective mass measured by the MFC method increased with increasing carrier concentration, and it varied within the range of $0.30–0.47m_e$ when n is lower than 7×10^{20} cm^{-3}. In this experiment, we could exactly measure m_d* in the bulk ZnO nanocomposite by using only two parameters, namely the temperature-dependent carrier concentration and the temperature-dependent Seebeck coefficient. From these results, it was manifested that the Seebeck coefficient in the degenerately doped ZnO nanocomposite follows the classical Pisarenko relation without any extra effect induced by the nanostructure.

The effect of the nanostructure in the nanocomposite was clearly corroborated in thermal conductivity (Fig. 5(a)). In this figure, lattice thermal conductivity (κ_L) was determined by using the Wiedemann–Franz law, $\kappa_L = \kappa - L\sigma T$, where L is the Lorentz number (2.45×10^{-8} V^2 K^{-2}). The thermal conductivity in the nanocomposite was at least 4-fold lower than those in conventionally prepared Al-doped ZnO materials.[4,20] The thermal conductivity in the nanocomposite was 7.6 W m^{-1} K^{-1} at room temperature and it monotonically decreased with increasing temperature ($\kappa_{1000K} < 2.0$ W m^{-1} K^{-1}). By using the Callaway formula, Kinemuchi *et al.* reported that the thermal conductivity in a ZnO nanocomposite can approach below 5 W m^{-1} K^{-1} at high temperature only if the grain size is less than 100 nm.[6] However, we observed the drastic reduction of the thermal conductivity in the nanocomposite whose grain size is around 200 nm. Recently, Jood *et al.* reported a very low thermal conductivity in a ZnO nanocomposite ($\kappa_{1000K} < 2.0$ W m^{-1} K^{-1}).[7] Although the grain size in the nanocomposite was no smaller than 1 μm, they could achieve the significant thermal conductivity reduction mainly due to the $ZnAl_2O_4$ nanoprecipitates and intergranular nanograins. This kind of thermal conductivity reduction by nanoprecipitates has also been widely reported for other thermoelectric material systems.[30–35] Therefore, the low thermal conductivity in this oxide nanocomposite was achieved not only by the nanograins in the nanocomposite, but also by the $ZnAl_2O_4$ nanoprecipitates. Furthermore, a plot of the lattice thermal conductivity *vs.* $1/T$ shows a good linearity, as shown in the inset of Fig. 5(a), indicating that Umklapp processes play a dominant role in the phonon scattering.[28,36–38]

The dimensionless figure of merit, ZT, of the degenerately Al-doped ZnO nanocomposite is shown in Fig. 5(b). The maximum ZT of 0.34 at 1073 K was achieved in the nanocomposite and it is a significantly enhanced value compared to Ohtaki *et al.*'s original report (0.30 at 1273 K).[4] Because the ZT value is a collective property of S, σ, and k at a temperature, understanding the effects of the nanocomposite on each parameter in ZT is of great importance for further improvement. As discussed above, the effects of the nanostructuring were mainly observed in the transport properties of electrons (σ) and phonons (κ) rather than the Seebeck coefficient due to the scattering at the nanograin boundaries and nanoprecipitates. It implies that the key factor for the enhancement in ZT is how much we can increase σ/κ by the nanostructuring. Therefore, the increase of σ/κ, by controlling the grain size, nanoprecipitate and carrier concentration in the nanocomposite, is strongly demanded for further enhancement in ZT. Moreover, the increase of S by nanostructuring, such as the carrier filtering effect by nanoprecipitates,[39,40] may provide a new pathway for the enhancement in the ZnO nanocomposite system.

Conclusions

A degenerately Al-doped ZnO nanocomposite was successfully fabricated by the spark plasma sintering of 2 mol% Al-doped ZnO nanoparticles, and its charge transport and thermoelectric properties were investigated. Firstly, the peculiar temperature-dependence of the Hall mobility was characterized in the nanocomposite mainly due to the grain boundary scattering of the electrons. Secondly, the carrier concentration was independent of the temperature, and it was the origin of the linear relationship between the Seebeck coefficient and temperature in the frame of the Pisarenko relation. The interpretation of these results provided us the density of the state effective mass ($m_d^* = 0.33m_e$) in the nanocomposite. Finally, we obtained a very low thermal conductivity of less than 2.0 W m^{-1} K^{-1} and it was due to the enhanced phonon scattering at nanograin boundaries and nanoprecipitates.

Acknowledgements

This research was supported by the Fundamental R&D Program for Core Technology of Materials (K0006007) funded by the Ministry of Knowledge Economy and also supported by the Nano Material Technology Development Program (2011-0030147) through the National Research Foundation of Korea (NRF) funded by the Ministry of Education, Science and Technology, Republic of Korea.

References

1 S. B. Riffat and X. Ma, *Appl. Therm. Eng.*, 2003, **23**, 913.
2 G. J. Snyder and E. S. Toberer, *Nat. Mater.*, 2008, **7**, 105.
3 J. R. Sootsman, D. Y. Chung and M. G. Kanatzidis, *Angew. Chem., Int. Ed.*, 2009, **48**, 8616.
4 M. Ohtaki, T. Tsubota, K. Eguchi and H. Arai, *J. Appl. Phys.*, 1996, **79**, 1816.
5 M. Ohtaki, K. Araki and K. Yamamoto, *J. Electron. Mater.*, 2008, **38**, 1234.
6 Y. Kinemuchi, H. Nakano, M. Mikami, K. Kobayashi, K. Watari and Y. Hotta, *J. Appl. Phys.*, 2010, **108**, 053721.
7 P. Jood, R. J. Mehta, Y. Zhang, G. Peleckis, X. Wang, R. W. Siegel, T. Borca-Tasciuc, S. X. Dou and G. Ramanath, *Nano Lett.*, 2011, **11**, 4337.
8 D. H. Zhang and H. L. Ma, *Appl. Phys. A: Mater. Sci. Process.*, 1996, **62**, 487.
9 A. Wang, J. Dai, J. Cheng, M. P. Chudzik, T. J. Marks, R. P. H. Chang and C. R. Kannewurf, *Appl. Phys. Lett.*, 1998, **73**, 327.
10 T. Yamada, H. Makino, N. Yamamoto and T. Yamamoto, *J. Appl. Phys.*, 2010, **107**, 123534.
11 K. Ellmer, *J. Phys. D: Appl. Phys.*, 2001, **34**, 3097.
12 B. D. Ahn, S. H. Oh, H. J. Kim, M. H. Jung and Y. G. Ko, *Appl. Phys. Lett.*, 2007, **91**, 252109.
13 Z. Zhou and Y. Deng, *J. Phys. Chem. C*, 2009, **113**, 19853.
14 R. Wahab, Y. S. Kim, K. Lee and H. S. Shin, *J. Mater. Sci.*, 2010, **45**, 2967.
15 H. Kim, A. Piqué, J. S. Horwitz, H. Murata, Z. H. Kafafi, C. M. Gilmore and D. B. Chrisey, *Thin Solid Films*, 2000, **377–388**, 798.
16 H. Kim, J. S. Horwitz, S. B. Qadri and D. B. Chrisey, *Thin Solid Films*, 2002, **420–421**, 107.
17 Z. A. Munir, U. Anselmi-Tamburini and M. Ohyanagi, *J. Mater. Sci.*, 2006, **41**, 763.
18 Y. Fujishiro, M. Miyata, M. Awano and K. Meada, *J. Am. Ceram. Soc.*, 2003, **86**, 2063.
19 K. F. Cai, E. Müller, C. Drašar and A. Mrotzek, *Mater. Sci. Eng., B*, 2003, **104**, 45.
20 T. Tsubota, M. Ohtaki, K. Eguchi and H. Arai, *J. Mater. Chem.*, 1997, **7**, 85.
21 J. W. Orton and M. J. Powell, *Rep. Prog. Phys.*, 1980, **43**, 1263.
22 J. Y. W. Seto, *J. Appl. Phys.*, 1975, **46**, 5247.
23 M. N. Islam and M. O. Hakim, *J. Phys. D: Appl. Phys.*, 1986, **19**, 615.
24 S. Ghosh, A. Sarkar, S. Chaudhuri and A. K. Pal, *Thin Solid Films*, 1991, **205**, 64.
25 J. Bruneaux, H. Cachet, M. Froment and A. Messad, *Thin Solid Films*, 1991, **179**, 129.
26 M. W. J. Prins, K.-O. Grosse-Holz, J. F. M. Cillessen and L. F. Feiner, *J. Appl. Phys.*, 1998, **83**, 888.
27 T. K. Gupta and W. G. Carlson, *J. Mater. Sci.*, 1985, **20**, 3487.
28 K. P. Ong, D. J. Singh and P. Wu, *Phys. Rev. B: Condens. Matter Mater. Phys.*, 2011, **83**, 115110.
29 W. M. Kim, I. H. Kim, J. H. Ko, B. Cheong, T. S. Lee, D. Kim and T.-Y. Seong, *J. Phys. D: Appl. Phys.*, 2008, **41**, 195409.
30 D. L. Medlin and G. J. Snyder, *Curr. Opin. Colloid Interface Sci.*, 2009, **14**, 226.
31 J. R. Sootsman, J. He, V. P. Dravid, C.-P. Li, C. Uher and M. G. Kanatzidis, *J. Appl. Phys.*, 2009, **105**, 083718.
32 Y. Lan, B. Poudel, Y. Ma, D. Wang, M. S. Dresselhaus, G. Chen and Z. Ren, *Nano Lett.*, 2009, **9**, 1419.
33 Y. Gelbstein, B. Dado, O. Ben-Yehuda, Y. Sadia, Z. Dashevsky and M. P. Dariel, *Chem. Mater.*, 2010, **22**, 1054.
34 Y. Pei, J. Lensch-Falk, E. S. Toberer, D. L. Medlin and G. J. Snyder, *Adv. Funct. Mater.*, 2011, **21**, 241.
35 C. Kang, H. Kim, S. Park and W. Kim, *Appl. Phys. Lett.*, 2010, **96**, 213114.
36 T. Tsubota, M. Ohtaki, K. Eguchi and H. Arai, *J. Mater. Chem.*, 1998, **8**, 409.
37 S. Katsuyama, Y. Takagi, M. Ito, K. Majima, H. Nagai, H. Sakai, K. Yoshimura and K. Kosuge, *J. Appl. Phys.*, 2002, **92**, 1391.
38 Ü. Özgür, Y. I. Alivov, C. Liu, A. Teke, M. A. Reshchikov, S. Doğan, V. Avrutin, S.-J. Cho and H. Morkoç, *J. Appl. Phys.*, 2005, **98**, 041301.
39 M. S. Dresselhaus, G. Chen, M. Y. Tang, R. Yang, H. Lee, D. Wang, Z. Ren, J.-P. Fleurial and P. Gogna, *Adv. Mater.*, 2007, **19**, 1043.
40 S. V. Faleev and F. Léonard, *Phys. Rev. B: Condens. Matter Mater. Phys.*, 2008, **77**, 214304.

